



Supplementary Materials for

Room-Temperature Quantum Bit Memory Exceeding One Second

P. C. Maurer, G. Kucsko, C. Latta, L. Jiang, N. Y. Yao, S. D. Bennett, F. Pastawski, D. Hunger, N. Chisholm, M. Markham, D. J. Twitchen, J. I. Cirac, M. D. Lukin*

*To whom correspondence should be addressed. E-mail: lukin@physics.harvard.edu

Published 8 June 2012, *Science* **336**, 1283 (2012)

DOI: 10.1126/science.1220513

This PDF file includes:

Materials and Methods
Supplementary Text
Figs. S1 to S12
References (31–44)

Supporting Material for

Room temperature quantum memory based upon a single nuclear spin

P. C. Maurer, G. Kucsko, C. Latta, L. Jiang, N. Y. Yao, S. D. Bennett, F. Pastawski,
D. Hunger, N. Chisholm, M. Markham, D. J. Twitchen, J. I. Cirac, and M. D. Lukin

I. MATERIALS AND METHODS

Sample

The sample used in this work is an unpolished ultra-pure diamond grown by chemical vapor deposition. The low substitutional nitrogen concentration of < 1 ppb and high isotopic ^{12}C purity of 99.99 % leads to electron spin coherence times T_{2e}^* long enough to sense a single ^{13}C nuclear spin via a hyperfine interaction of a few kHz.

Optical Setup

The sample is mounted on a xyz-piezoelectric stage in the focal plane of a home-build confocal microscope with a Nikon Plan Fluor 100x oil immersion objective ($N_A = 1.3$). To suppress decoherence of the electronic spin due to external magnetic field fluctuations the microscope is placed inside a μ -metal shield. The magnetic shielding reduces ambient DC fields by a factor of 80 and suppressed AC fields to better than $40 \mu\text{G}$. This allows us to obtain NV electronic spin coherence times of $T_2^* = (470 \pm 100) \mu\text{s}$. This value agrees well with the linear scaling of T_2^* of the electronic spin as a function of the ^{13}C concentration [14].

Excitation of the NV center is performed by a frequency doubled YAG laser ($\lambda = 532 \text{ nm}$) using 1.4 mW power corresponding to three times the saturation power. The NV center fluorescence is emitted into the phonon sideband (630-800). The emitted fluorescence beam is separated from the excitation by a dichroic filter and an appropriate long pass filter. The fluorescence beam is then focused onto an avalanche photodiode (APD) after passing a pinhole for confocal microscopy. Short laser pulses are generated by an accusto-optical modulator (AOM) from Isomet in a double pass geometry. The rise time of the AOM is adjusted to be approximately 20 ns. A second, strong (30 mW), green laser beam is coupled into the beam path by a 50/50 polarizing beam splitter cube.

To avoid leakage from the shut-off 30 mW beam a mechanical shutter from Thorlabs (switching time ≈ 10 ms) was employed.

Microwave and RF Setup

To coherently drive the electronic spin of the NV center we deliver microwaves to the sample by a transmission line fabricated on a glass coverslip, glued to the diamond sample. To perform pulsed microwave manipulation of the electronic spin we use peak powers of 10 W allowing us to manipulate the electronic spin with a Rabi frequency on the order of $(2\pi)40$ MHz.

To manipulate the ^{13}C nuclear spin using high power radio frequency, a lithographically patterned micro-coil is fabricated on an alumina substrate [31]. In order to prevent excessive ohmic loss the conductors are then plated with copper in a SU-8 mold to a thickness of around $40\ \mu\text{m}$ allowing peak powers of several hundred watts. To ensure maximal nuclear Rabi frequency the RF-coil is aligned in such a way that the ac RF field of the coil is perpendicular to the external dc magnetic field. This allows us to manipulate our ^{13}C nuclear spin with Rabi frequencies of $\approx (2\pi)100$ kHz.

II. PHOTON COUNTING STATISTICS AND READOUT FIDELITY

In this part of the supplementary information we discuss the statistics of detected photons during a repetitive readout of the nuclear spin for a certain integration time. First, we derive an analytical expression for the statistical distribution of the detected photons that is fitted to the data in Fig. 2c of the main text. We then analyze the readout and initialization fidelity derived from these distributions.

Photon counting statistics

We start by first pointing out that the probability $p^{(n)}$ for n quantum jumps during the integration window τ is Poissonian-distributed with $p^{(n)} = \frac{\lambda^n}{n!} \exp(-\lambda)$, where $\lambda = \tau/T_{1n}$ and $1/T_{1n}$ is the nuclear depolarization rate. For an integration time of $\tau = 4.4$ s (Fig. 2c of the main text and Fig. S1a) and a nuclear spin flip time $T_{1n} = 25$ s, the probability for no quantum jump during readout is $p^{(0)} = 83.8\%$. The probability for one quantum jump is $p^{(1)} = 14.8\%$ and $p^{(n>1)} = 1\%$

for more than one jump. This allows us to restrict the discussion to the case where either zero or one quantum jump takes place during the readout time.

For no quantum jump event during the readout τ , the photon count statistics $\alpha_s^{(0)}$ is Gaussian:

$$\alpha_s^{(0)}(x) = \frac{1}{\sqrt{2\pi\mu_s}} \exp\left(-\frac{(x - \mu_s)^2}{2\mu_s}\right), \quad (\text{S1})$$

where μ_s is the average photon count rate for the nuclear spin in the $|s = \downarrow (\uparrow)\rangle$ state and x is the number of detected photons. For the shot-noise limited detection, we take the standard deviation $\sigma_s = \sqrt{\mu_s}$.

In the case of a single quantum jump event, the number of detected photons $\alpha_s^{(1)}$ will no longer be Gaussian distributed. We note that conditioned on one quantum jump occurring during the readout interval τ , the time spent in $|s\rangle$ will be uniformly distributed. Hence the number of counted photons is given by $\mu \sim \mu_\downarrow + (\mu_\uparrow - \mu_\downarrow)Unif$, where $Unif$ denotes the uniform distribution on the interval $(0, 1)$. Taking into account the photon shot noise, we find the statistics of detected photons conditional on a single nuclear spin flip:

$$\begin{aligned} \alpha^{(1)}(x) &= \frac{1}{\mu_\uparrow - \mu_\downarrow} \int_{\mu_\downarrow}^{\mu_\uparrow} d\mu \frac{1}{\sqrt{2\pi\mu}} \exp\left(-\frac{(x - \mu)^2}{2\mu}\right) \\ &\approx \frac{1}{2(\mu_\uparrow - \mu_\downarrow)} \left(\text{Erf}\left(\frac{\mu_\downarrow - x}{\sqrt{2\mu_\downarrow}}\right) - \text{Erf}\left(\frac{\mu_\uparrow - x}{\sqrt{2\mu_\uparrow}}\right) \right), \end{aligned} \quad (\text{S2})$$

which is independent of the initial nuclear spin state $|s\rangle$.

Combing eq. (S1), (S2) we can find an analytical expression for the photon counting statistics:

$$\alpha_s(x) \approx p^{(0)}\alpha_s^{(0)}(x) + p^{(1)}\alpha^{(1)}(x). \quad (\text{S3})$$

In Fig. 2c of the main text we fit this function to the recorded photon counting statistics with $\mu_{\downarrow(\uparrow)}$ being fit parameters. The measured data is in excellent agreement with our model of Fig. 2c and S1a.

Readout and initialization fidelity

As discussed in the main text we define the readout fidelity $\eta_\downarrow(n_{thr})$ by the probability of being in nuclear spin $|\downarrow\rangle$ conditional on detecting a photon number smaller than a threshold n_{thr} . The readout fidelity $\eta_\downarrow(n_{thr})$ is then defined as

$$\eta_\downarrow(n_{thr}) = \frac{P_\downarrow(n_{thr})}{P_\downarrow(n_{thr}) + P_\uparrow(n_{thr})}, \quad (\text{S4})$$

where $P_{\downarrow(\uparrow)}(n_{thr}) = \int_0^{n_{thr}} \alpha_{\downarrow(\uparrow)}(x)dx$ is the probability that for nuclear spin \downarrow (\uparrow) the number of detected photons is below n_{thr} , and vice versa for $\eta_{\uparrow}(n_{thr})$. For optimal readout fidelity η the threshold n_{thr} is chosen in such a way that $\eta_{\downarrow(\uparrow)}$ is maximized.

The readout fidelity η is determined by initializing the nuclear spin in a known state \downarrow (\uparrow) and consecutively reading it out with our single shot measurement. The readout (20,000 repetitions) allows us then to determine the photon counting distribution depending on the initial state and hence the fidelity η .

This relies on a high initialization fidelity of the nuclear spin to the desired state. To initialize the nuclear spin we perform a repetitive readout. If the recorded counts are smaller than a threshold n_{thr}^{\downarrow} we assign the nuclear spin to $|\downarrow\rangle$ if they are larger than n_{thr}^{\uparrow} we assign $|\uparrow\rangle$. In principle this allows for initialization with fidelity well above 99 %. In Fig. S1b we plot the initialization fidelity as a function of the threshold n_{thr}^{\downarrow} and n_{thr}^{\uparrow} . For a threshold of 147(195) counts we can initialize the nuclear spin state with a fidelity of $\approx 97\%$.

III. READOUT OF THE ^{13}C NUCLEAR SPIN

This section discusses the details of the ^{13}C readout. We first show that the electron Ramsey fringes can be described by a single sine-function due to dynamical polarization of the ^{14}N nuclear spin. We then discuss the dependence of the fluorescence signal on the detuning from the ESR transition and the implication on the readout fidelity. Finally we give an explanation on how we normalized the results of the repetitive readout.

Throughout this paper we neglect the ^{14}N nuclear spin of the NV center. This is justified since we work at a field of ~ 244 Gauss, which is sufficiently close to the excited state level-anti-crossing at 500 Gauss to dynamically polarize the ^{14}N nuclear spin [32]. As shown in Fig. S2a the nitrogen nuclear spin is polarized to 71 % leaving us with nearly sinusoidal Ramsey fringes (Fig. S2b).

As discussed in the main text, our readout scheme relies on the acquisition of a phase difference, depending on the nuclear spin state, in an electron Ramsey experiment over a free precession time τ . The fluorescence rate for this Ramsey experiment is given by

$$F_{\tau}(m_I, \delta) = f^0 - (f^0 - f^1) \frac{1 + e^{-\tau/T_2^*} \cos((\delta + m_I A_{\parallel})\tau)}{2}, \quad (\text{S5})$$

where $f^{0(1)}$ denotes the fluorescence rate of the electronic spin of the NV center in the $m_s = 0(1)$

state, A_{\parallel} the parallel component of the hyperfine interaction, m_I the spin projection of the ^{13}C nuclear spin ($m_I = \pm 1/2$), δ the detuning of the microwave field from resonance and T_2^* the coherence time of the electronic spin.

In our readout, we set the Ramsey precession time τ to $\tau = \frac{\pi}{A_{\parallel}}$. The fluorescence rate for the readout then simplifies to

$$F(m_I, \delta) = \frac{f^0 + f^1}{2} + e^{-\tau/T_2^*} (f^0 - f^1) m_I \sin\left(\frac{\delta}{A_{\parallel}} \pi\right). \quad (\text{S6})$$

The readout signal of the nuclear spin state is therefore modified by an additional factor of $\sin(\pi\delta/A_{\parallel})$. Since in our experiment $A_{\parallel} = (2\pi)2.7$ kHz, resonance frequency drifts of only a kilohertz are sufficient to affect the readout contrast and hence reduce the readout fidelity. Indeed, we observe fluctuations of the readout contrast on a timescale of ~ 30 min as shown in Fig. S3. One source for such drifts likely originates from the strong temperature dependence of the zero field splitting of NV^- , which has been measured [21] to be around $(2\pi)74 \frac{\text{kHz}}{\text{K}}$.

When $\delta(t)$ is unknown it is impossible to uniquely determine the orientation of the nuclear spin with respect to the external magnetic field. Nevertheless if the correlation time of $\delta(t)$ is much larger than the typical duration of an individual experiment we can still use our readout process to define a qubit state. We redefine for each experimental run the basis in which our nuclear spin is measured such that low (high) fluorescence corresponds to $|\downarrow\rangle$ ($|\uparrow\rangle$).

In general, a measurement consists of a repetitive readouts c_1 , a pulse sequence and another repetitive readout c_2 , where c_1 initializes the nuclear spin in a state $|s\rangle$ and c_2 reads out the nuclear spin after applying a pulse sequence. In Fig. 4c, additional repetitive readouts were performed in order to normalize the signal.

In Fig. 1c of the main text, we measure the nuclear spin flip probability p induced by an RF π -pulse, as a function of frequency ω . In this experiment, we first initialize the nuclear spin to $|\downarrow\rangle$ via a projective measurement c_1 (See Fig. 1c of the main text). After initialization, we apply an RF-pulse with frequency ω before reading it out in c_2 . To normalize our data, we measure two additional references (c_3, c_4). The measurement c_3 initializes the nuclear spin to $|\downarrow(\uparrow)\rangle$ and c_4 reads it out. The RF induced transition probability p is then

$$p = \frac{\zeta_2^{\downarrow} - \zeta_4^{\downarrow}}{\zeta_4^{\uparrow} - \zeta_4^{\downarrow}}, \quad (\text{S7})$$

where ζ_i^s is the number of counted photons during readout c_i conditional on the nuclear spin being in $|s\rangle$.

The data in Fig. 4c are normalized in a similar fashion with an additional RF π -pulse prior to readout c_4 . In addition, before reading out the nuclear spin with our single shot readout we incorporated waiting times of 10 s. This is necessary since heating due to dissipation of the laser reduces the readout contrast for measurement c_2 and hence reduces the fidelity.

Fig. 3b,c of the main text show the decay time for a Ramsey signal with (without) simultaneous green excitation. In these experiments, no references are measured. Therefore, we normalize the data such that the fitted curves start with full contrast. This is justified under the assumption that for zero duration of storage time no dephasing/decay occurs.

In Fig. 4a we perform a similar normalization by a constant factor. Using this normalization we can reduce the data acquisition time by more than a factor of two (2 weeks of averaging) by removing the references and reducing the waiting time between laser excitation and readout. The results of this procedure agree well with the fidelity measured from process tomography where no such normalization is performed.

IV. NUCLEAR COHERENCE AND DEPolarIZATION

In this part of the supplementary information we will use the spin-fluctuator model to obtain the dephasing and depolarization rates of the nuclear spin under green illumination. The spin-fluctuator model consists of the nuclear qubit (spin) and the NV electron environment (fluctuator). The nuclear spin evolves coherently while the fluctuator undergoes incoherent stochastic transitions between different levels. Such evolution of the fluctuator induces decoherence of the spin.

We will first study a simple spin-fluctuator model, for which we can obtain analytic expressions for the nuclear spin dephasing and depolarization rates that qualitatively explain the experimental data. Then, we consider a specific model with 11 levels for fluctuator dynamics, which can be solved using master equations and compared with the experimental data.

Spin-fluctuator model

The Hamiltonian associated with the nuclear spin is

$$H_n = (\gamma^{13C}B)\hat{I}_z + \sum_{\alpha,\beta=x,y,z} A_{\alpha,\beta}\hat{S}_\alpha\hat{I}_\beta \quad (\text{S8})$$

which consists of the Zeeman splitting due to external magnetic field ($\gamma_{13C}B$) and the dipole interaction with the electronic spin ($A_{\alpha,\beta}$). In this simple model we assume that under strong green illumination the electronic spin fluctuates between the states $m_s = \pm\frac{1}{2}$. We approximate the effective Hamiltonian as

$$H_n = (\gamma_{13C}B)\hat{I}_z + f(t) \sum_{\beta=x,y,z} A_{z,\beta}\hat{I}_\beta, \quad (\text{S9})$$

where we replaced \hat{S}_z by the time-dependent gaussian stochastic variable $f(t) = \{-\frac{1}{2}, \frac{1}{2}\}$ described by a Bernoulli process and neglected other terms associated with \hat{S}_x and \hat{S}_y . For simplicity, we assume that $\langle f(t) \rangle = 0$ and the correlation function is

$$\langle f(t)f(0) \rangle = \langle f^2(0) \rangle e^{-2\gamma|t|} = \frac{1}{4}e^{-2\gamma|t|}, \quad (\text{S10})$$

where γ is the forward/backward effective transition rate controlled by the laser intensity.

We may rewrite the Hamiltonian as

$$H_n = (\gamma_{13C}B)\hat{I}_z + f(t) \left(A_{z,z}|\hat{I}_z + A_{z,+}\hat{I}_+ + A_{z,-}\hat{I}_- \right) \quad (\text{S11})$$

with $\hat{I}_\pm = (I_x \pm iI_y)$ and $A_{z,\pm} (= A_{z,\mp}^*) = (A_{z,x} \mp iA_{z,y})/2$.

Dephasing. We can estimate the nuclear spin dephasing rate (T_2 process) induced by the terms $A_{z,z}(t)\hat{I}_z$. For time T , the random phase accumulated by the nuclear spin is given by $\Phi_{FID} = \int_0^T A_{z,z}(t) dt$. Assuming Gaussian noise we can compute the expectation value of the nuclear coherence, we have

$$\langle e^{i\Phi_{FID}} \rangle = e^{-\frac{1}{2}\langle \Phi_{FID}^2 \rangle} \approx e^{-T/T_{FID}}, \quad (\text{S12})$$

where

$$1/T_{FID} = \frac{A_{\parallel}^2}{8\gamma}, \quad (\text{S13})$$

because $\frac{1}{2}\langle \Phi_{FID}^2 \rangle = \frac{1}{2} \int_0^T dt \int_0^T dt' A_{z,z}^2 \langle f(t)f(t') \rangle \approx \frac{1}{2} \int_0^T dt \int_{-\infty}^{\infty} d\tau A_{z,z}^2 \langle f(\tau)f(0) \rangle = \frac{A_{z,z}^2 T}{8\gamma}$ and $A_{\parallel} = A_{z,z}$. For our system, γ increases with the laser intensity, and consequently T_{FID} increases with the laser intensity, which is related to the motional averaging effect in NMR.

Depolarization. We can estimate the nuclear spin depolarization rate (T_1 process) induced by the terms $f(t) \left(A_{z,+}\hat{I}_+ + A_{z,-}\hat{I}_- \right)$. Noting that $|A_{z,+}| = |A_{z,-}| \equiv A_{\perp}/2$, we can re-express the noise as, $A_{\perp}f(t)I_x$. First order time-dependent perturbation theory yields the transition rates in the two directions as [34]:

$$\Gamma_{\uparrow} = \left(\frac{A_{\perp}}{2} \right)^2 S_q(-\gamma_{13C}B) \quad \text{and} \quad \Gamma_{\downarrow} = \left(\frac{A_{\perp}}{2} \right)^2 S_q(\gamma_{13C}B) \quad (\text{S14})$$

where $S_q(\omega)$ is the noise spectral density. Assuming classical telegraph noise, $\Gamma_{\uparrow} = \Gamma_{\downarrow} = \frac{A_{\perp}^2}{16} \frac{\gamma}{(\gamma_{13C}B/2)^2 + \gamma^2}$, yielding a depolarization rate,

$$1/T_{1n} = \Gamma_{\uparrow} + \Gamma_{\downarrow} = \frac{A_{\perp}^2}{8} \frac{\gamma}{(\gamma_{13C}B/2)^2 + \gamma^2}. \quad (\text{S15})$$

Depolarization in the dark. Without laser excitation, the nuclear spin lifetime is no longer limited by the optically induced depolarization given in eq. (S15). Instead, in this regime, the dominant contribution to T_{1n} is expected to be coherent dipole-dipole interactions, $H_{dd} = D_{dd} (3(\mathbf{I} \cdot \mathbf{n})(\mathbf{I}' \cdot \mathbf{n}) - \mathbf{I} \cdot \mathbf{I}')$ between the memory spin \mathbf{I} and neighboring ^{13}C nuclear spins \mathbf{I}' . In our present experiment D_{dd} is on the order of 1 Hz. However, when the dephasing rate of the nuclear spin is much large than that of coherent interactions (D_{dd}), spin-flips are suppressed. In this case, commonly denoted as the quantum-Zeno effect [35], the nuclear polarization, n_{\uparrow} , is characterized by an exponential decay as a function of time,

$$n_{\uparrow}(t) = \frac{1}{2} (1 + \exp(-\frac{(D_{dd}/(2\pi))^2}{1/T_{1e}}t)). \quad (\text{S16})$$

The measurement in Fig. S4 depicts the nuclear spin dependent fluorescence rate as a function of waiting time t between initialization and readout. The data indicate that for $t < 3$ min no noticeable decay in the nuclear spin polarization is evinced.

Detailed Model

While the above simplified model captures the basic idea of the motional averaging in our system the discussed two level scheme is an oversimplification in the case of NV centers. To discuss the effects of an applied optical drive to the full extent we choose a different approach. For this we incorporate 11 levels for the electronic state and the two levels for the ^{13}C nuclear spin as shown in Fig. S5. Using a master equation we can simulate the nuclear decoherence. For the numerical solution of the master equation we assumed a secular approximation for the nuclear and electronic spin leaving us with an effective Hamiltonian for the hyperfine interaction $H_{hyp} = (A_{\parallel}I_z + A_{\perp}I_x) S_z$, which is justified since $A \ll g_e\mu_B B$. Moreover, we neglect any coherence between electronic states since all our fields are classical.

A solution of the master equation for the nuclear coherence time is shown in Fig. S6a. As expected the coherence time scales linearly as a function of laser intensity when exceeding optical saturation. Furthermore at small laser intensities ($I \sim I_{sat}/1000$, with I_{sat} the saturation intensity)

the coherence time has a local maximum originating from repolarization of the electronic spin without deionizing the NV center. This is possible to a certain extent since the (de)ionization process is a two photon process but the repolarization rate is linear in laser intensities for $I \ll I_{sat}$.

Even though the simplified two level model is able to qualitatively explain the linear scaling of the coherence as a function of laser intensity it does not quantitatively reproduce the T_2 (dashed-dotted black line). The deviation from the two level model originates from the fact that at large laser intensities other states beside the $m_s = 0$ and $m_s = \pm 1/2$ can be occupied.

Next we compare the solution of the master equation with the slope extracted from the experimental data in Fig. 3e of the main text. The slope is shown in Fig. S6a by a dashed red line. The experimental data is in excellent agreement with the simulation based on the transition rates given in the caption of Fig. S5 .

Since we know that this master equation allows us to quantitatively reproduce T_{2n} we can use the master equation to estimate a value for the perpendicular component of the hyperfine interaction A_{\perp} . Optimizing our fit we can find A_{\perp} to be on the order of $(2\pi)1.8$ kHz as shown in Fig. S6b. Except for laser intensities $\ll I_{sat}$ the simulated T_{1n} times agree well with the measured data. Plugging $A_{\perp} = (2\pi)1.8$ kHz into the two level model in eq. (S15) yields a theoretical curve (black dashed-dotted line) showing a significant discrepancy with the measured data. If we neglect the contact term [36] of the hyperfine interaction A and assume only dipolar interaction we can estimate the distance between the electronic spin and the nuclear spin to be approximately 1.7 nm.

Nevertheless, our simplified two level model from eq. (S13) and (S15) allows us by rescaling the hyperfine interaction and the (de)ionization rate γ to find effective rates that quantitatively reproduce the T_{1n} and T_{2n} times. As shown in Fig. 2d and 3e using the rates $A_{\parallel}^{\text{eff}} = (2\pi)3.3$ kHz, $A_{\perp}^{\text{eff}} = (2\pi)1.0$ kHz and $\gamma = (2\pi)150 \times P_{\text{Laser}}$ kHz/mW reproduce the measured T_{1n} and T_{2n} as function of the laser power P_{Laser} .

V. NUCLEAR DECOHERENCE UNDER DYNAMICAL DECOUPLING

Figure 3d in the main text shows that the nuclear coherence time is significantly extended under the application of MREV-8, which suppresses the nuclear dipole-dipole interaction. Here we provide further details on MREV-8 and identify the sources of residual decoherence.

MREV-8 dynamical decoupling

The Waugh, Huber and Haberlen four-pulse sequence (WHH), shown in Fig S7a, decouples nuclear dipole-dipole interactions [37]. In our experiment we use the MREV-8 sequence, shown in Fig S7b, which is an eight-pulse sequence made up of WHH cycles of alternating phase.

The effect of MREV-8 on the dipole-dipole interaction can be understood using average Hamiltonian theory [37]. We describe the effects of the pulses by moving to an interaction picture (i.e. the toggling frame) with respect to the Hamiltonian defined by the $\pi/2$ rotations. Provided the characteristic frequencies ω of H satisfy $\omega t \ll 1$ we can perform a Magnus expansion, and describe the total time evolution during the cycle is described by an effective Hamiltonian,

$$H_{\text{eff}} = H^{(0)} + H^{(1)} + H^{(2)} + \dots \quad (\text{S17})$$

where the first few terms are

$$H^{(0)} = \sum_{j=1}^M H_j, \quad (\text{S18})$$

$$H^{(1)} = \frac{-i\tau}{2M} \sum_{k>j}^M \sum_{j=1}^M [H_k, H_j]. \quad (\text{S19})$$

Here, M is the total number of time intervals of length τ between pulses as shown in Fig S7, and H_j is the interaction picture Hamiltonian in the toggling frame in interval j . The zeroth order effective Hamiltonian is just the average over the cycle in the toggling frame, and the n th terms in the expansion consist of nested commutators of order n .

Our goal is to find the effect of MREV-8 on the nuclear dipole-dipole interaction within secular approximation,

$$H_D = \sum_{j>k} D_{jk} (3I_j^z I_k^z - \mathbf{I}_j \cdot \mathbf{I}_k), \quad (\text{S20})$$

where the dipolar coupling frequency is $D_{jk} = \hbar^2 \gamma_n^2 [1 - 3 \cos^2(\theta_{ij})] / r_{ij}^3$, and the memory nuclear spin is indexed by $j = 0$. The effective, average Hamiltonian is obtained in terms of the zeroth order effective spin operators under MREV-8,

$$I_x^{(0)} = \frac{2}{3} I_x \quad I_y^{(0)} = \frac{1}{3} I_y \quad I_z^{(0)} = \frac{1}{3} (I_x + I_z). \quad (\text{S21})$$

Applying Eq. (S21) to each nuclear spin, one immediately finds that the average dipole-dipole Hamiltonian is $H_D^{(0)} = 0$. Furthermore, from the first order term in the Magnus expansion of

Eq. (S18) one finds that there is no first order correction, i.e. $H_D^{(1)} = 0$. Thus the leading order correction from the dipolar interaction is $(D\tau)^2 D \sim 10^{-4}$ Hz. Due to this very high suppression we expect that nuclear dipolar coupling alone cannot account for the residual decoherence when MREV-8 is applied. Next we discuss the sources of residual decoherence in the limits of low and high laser power.

Effect of MREV-8 on decoherence from NV ionization

At low laser power, nuclear decoherence is dominated by the (de)ionization of the NV electronic spin as described by the fluctuator model in Section IV. Here we find the effect of MREV-8 on this source of decoherence; for simplicity we consider a simple two-state model. Within this model, the Hamiltonian of the nuclear memory spin is

$$H_A = f(t) [A_{\parallel} I_z + A_{\perp} (I_x \cos \phi + I_y \sin \phi)], \quad (\text{S22})$$

where $f(t)$ describes telegraph noise with switching rate γ . In the absence of MREV-8 it is straightforward to calculate the resulting decoherence. A Fermi's golden rule calculation yields the depolarization rate in the limit $\gamma \gg \omega_L$,

$$\Gamma_1 = \frac{1}{8\gamma} A_{\perp}^2, \quad (\text{S23})$$

which is set by the coefficients of I_x and I_y . We calculate the dephasing rate within the Gaussian approximation, justified since $A_{\parallel}\tau \ll 1$, yielding

$$\Gamma_{\phi} = \frac{1}{8\gamma} A_{\parallel}^2, \quad (\text{S24})$$

which is set by the coefficient of I_z .

Next we find how MREV-8 modifies the decoherence from NV ionization. Here we cannot apply average Hamiltonian theory because the Hamiltonian fluctuates rapidly between $\pi/2$ pulses. Nonetheless, we can make use of the fast switching rate, since in the relevant limit $\gamma\tau \gg 1$, the fluctuations $f(t)$ are uncorrelated between one interval and the next. As a result, the total decoherence rate during one cycle is simply the incoherent average of the decoherence rates during each interval. The total dephasing rate is thus $\Gamma_{\phi} = \frac{1}{M} \sum_j^M \Gamma_{\phi,j}$ and the depolarization rate is $\Gamma_1 = \frac{1}{M} \sum_j^M \Gamma_{1,j}$, where the rates during each interval j are obtained from the Hamiltonian H_j in

the toggling frame, and using the same calculations as described above in the absence of MREV-8. When MREV-8 is applied we obtain

$$\Gamma_\phi = \frac{1}{24\gamma} [A_\parallel^2 + 2A_\perp^2 \sin^2 \phi], \quad (\text{S25})$$

$$\Gamma_1 = \frac{1}{24\gamma} [A_\perp^2 + 2(A_\parallel^2 + A_\perp^2 \cos^2 \phi)]. \quad (\text{S26})$$

The coefficients which previously led to pure dephasing or depolarization become mixed due to the $\pi/2$ rotations of MREV-8.

The total transverse decoherence rate $\Gamma_2 = 1/T_2$ includes contributions from both dephasing and depolarization, and can be approximated by $\Gamma_2 = \frac{1}{2}\Gamma_1 + \Gamma_\phi$. From the above results the total decoherence rates with and without MREV-8 are

$$\Gamma_2 = \frac{1}{8\gamma} \left[A_\parallel^2 + \frac{1}{2}A_\perp^2 \right] \quad (\text{without MREV-8}) \quad (\text{S27})$$

$$\Gamma_2 = \frac{1}{8\gamma} \left[\frac{2}{3}A_\parallel^2 + \frac{1}{2}A_\perp^2 \left(1 + \frac{2}{3} \sin^2 \phi \right) \right] \quad (\text{with MREV-8}) \quad (\text{S28})$$

From the fit of our T_1 data (see Fig. 2d in main text) we found $A_\perp/2\pi \sim 1.0$ kHz and $\gamma/2\pi \sim 300$ kHz. Using this value of γ , our T_2 data (see Fig. 3e in main text) this yields $A_\parallel/2\pi \sim 3.3$ kHz. Inserting these values into Eqs. (S27) and (S28) we find that the slope of T_2 versus laser power, at low power, is expected to be a factor $\sim 3/2$ larger when MREV-8 is applied. This simple estimate predicts that the decoherence from NV ionization is only slightly affected by MREV-8, in qualitative agreement with the data (see Fig. 3e of main text). However, the data shows that the impact of MREV-8 on the decoherence at low power is even smaller than the above prediction. This implies that in practice the total decoherence is slightly larger than obtained by incoherently averaging over each time interval, and as a result MREV-8 has almost no impact on the decoherence at low power.

Residual decoherence due to finite detuning

Lastly, we consider the residual decoherence under MREV-8 at high laser power where the ionization-induced decoherence is suppressed by motional averaging. As discussed above, decoherence due solely to the dipolar interaction is strongly suppressed by MREV-8, in particular the terms in the effective Hamiltonian to zeroth and first order in $D\tau$ vanish. However, the presence of small but finite detuning of our RF pulses leads to slightly imperfect dipolar cancelation; for

the longest times measured, this small detuning is sufficient to reintroduce the dipolar Hamiltonian through cross terms. This combined effect appears at first and higher orders in the effective Hamiltonian and sets the limit on T_2 in the present experiment.

Before discussing the combined effect of detuning and dipolar coupling, we consider the possibility of decoherence due to the detuning alone, in the absence of the dipolar interaction. The frequency resolution of our RF pulses is ~ 10 Hz, which means that a finite detuning of this order is expected. Constant detuning has no direct consequence since it is echoed out by the CPMG sequence in which MREV-8 is embedded. However, slow drifts in the detuning on the order of this frequency resolution could in principle lead to decoherence. From a measurement of $\delta(t)$ we estimate the rms fluctuation amplitude of $\delta_{\text{rms}}/2\pi \sim 10$ Hz and correlation time of $T_c \sim 350$ s. Estimating the impact of MREV-8 using the zeroth order term in Eq. (S18), we modify this by $\delta_{\text{rms}} \rightarrow \delta_{\text{rms}}/3$. Using these values and estimating $T_2 \sim \sqrt[3]{12N^{2/3}T_c(2\pi/\delta_{\text{rms}})^2}$ for pure dephasing [38] we find $T_2 \sim 27$ s from the detuning fluctuations. This suggests that slow detuning fluctuations are not directly the cause of the observed residual decoherence.

We now turn to the combined effect of finite detuning and dipolar coupling which appears to dominate the residual decoherence observed at high laser power. Dipolar coupling is described by Eq. (S20), and the Hamiltonian due to finite detuning δ is

$$H_\delta = -\delta \sum_j I_z^j \quad (\text{S29})$$

in the frame rotating at the RF frequency. Applying the Magnus expansion of Eq. (S18) the n th term in the effective Hamiltonian contains frequencies of order

$$\omega_n = [(\delta + D)\tau]^n (\delta + D). \quad (\text{S30})$$

For the longest coherence times measured, the interval between $\pi/2$ pulses is $\tau_{\text{max}} \sim 20$ ms, which yields $\delta\tau_{\text{max}} \sim 1$. Accordingly, we can no longer truncate the Magnus expansion to low order; specifically, the terms $(\delta\tau)^n D$ contribute to high order. This is the most important term, because terms involving only δ are echoed out by CPMG. Thus the effective decoherence time is set by the value of τ for which $\delta\tau \sim 1$. We have performed a simple numerical calculation to support this conclusion. In Fig. S8 we show the signal calculated using parameters provided in the caption. We obtain an effective $T_2 \sim 2$ s, in good agreement with the experiment.

Limits to coherence time

The lifetime of our proposed nuclear spin quantum memory is limited by a combination of optically induced dephasing, Γ_{opt} (eq. S13), and interactions with the remaining spins in the surrounding ^{13}C environment, Γ_{bath} . Since Γ_{opt} is proportional to A^2 , a slight reduction in strength of the hyperfine interaction increases the coherence time significantly. Upon reducing the ^{13}C concentration by an order of magnitude, it is possible to initialize and readout a nuclear spin coupled with strength, $A \sim (2\pi)0.5$ kHz. Furthermore, lowering the ^{13}C concentration will also result in a reduction of the nuclear-nuclear induced decoherence, that scales quadratically with the ^{13}C concentration.

As discussed in the maintext, the use of even higher laser intensities in our present setup is limited by heating of the diamond sample, which causes drifts in the ESR transition. However, by increasing the laser intensity while simultaneously cooling the diamond sample, it is possible to further enhance the coherence time. Finally, by decoupling the memory nuclear spin from the environment via composite MREV-8 pulses, we can suppress dipole-dipole interactions with the spin bath by up to three order of magnitudes [2]. The expected coherence time for this process as a function of ^{13}C concentration and laser power is plotted in Fig. S9, where we have assumed that heating is suppressed by feedback cooling. As shown, coherence times exceeding 1 min are easily achievable, while coherence times in the range of 1 hour are eminently feasible.

VI. PROCESS TOMOGRAPHY AND FIDELITY

In this section we will in detail discuss how the performance of our memory is measured. For this we will first explain the way we characterize the system's evolution using process tomography. Finally we will discuss our quantum memory in terms of fidelity.

To analyze the performance of our quantum memory we are interested in the full evolution of the ^{13}C nuclear spin during the storage process. One way to fully characterize the system's evolution $\mathcal{E}(\rho)$ is given by the Kraus map

$$\mathcal{E}(\rho) = \sum_{i,j=0}^{d^2-1} \chi_{i,j}(t) A_i \rho A_j^\dagger, \quad (\text{S31})$$

with ρ being the density matrix describing our ^{13}C nuclear memory, A_i a basis of operators acting on ρ and $d = 2$ the dimension of our system. The matrix χ is positive hermitian, time dependent

and fulfills the trace-preservation relation $\mathbb{1} = \sum_{i,j} \chi_{i,j} A_i A_j^\dagger$.

For $d = 2$ we have to determine 12 parameters which determine χ . Process tomography is a tool to measure these parameters by preparing the nuclear spin in 4 different basis states ($|\downarrow\rangle$, $|x\rangle$, $|y\rangle$ and $|\uparrow\rangle$), with $|x\rangle = (|\downarrow\rangle + |\uparrow\rangle)/\sqrt{2}$ and $|y\rangle = (|\downarrow\rangle + i|\uparrow\rangle)/\sqrt{2}$ followed by a state tomography after a certain storage time (Fig. S10)

For the given states, we can reconstruct a matrix $\tilde{\chi}$ that fulfills the Kraus map from eq. (S31). In the basis $A_i = \{\mathbb{1}, \sigma_x, \sigma_y, \sigma_z\}$ the matrix $\tilde{\chi}$ can be reconstructed by using the linearity of \mathcal{E} and the identity

$$\begin{aligned} \rho'_1 &= \mathcal{E}(|\downarrow\rangle\langle\downarrow|); \rho'_4 = \mathcal{E}(|\uparrow\rangle\langle\uparrow|) \\ \rho'_2 &= \mathcal{E}(|x\rangle\langle x| - i|y\rangle\langle y|) - \frac{(1-i)}{2}(\rho'_1 + \rho'_4) \\ \rho'_3 &= \mathcal{E}(|x\rangle\langle x| + i|y\rangle\langle y|) - \frac{(1+i)}{2}(\rho'_1 + \rho'_4) \\ \tilde{\chi} &= \frac{1}{4} \begin{pmatrix} \mathbb{1} & \sigma_x \\ \sigma_x & -\mathbb{1} \end{pmatrix} \begin{pmatrix} \rho'_1 & \rho'_2 \\ \rho'_3 & \rho'_4 \end{pmatrix} \begin{pmatrix} \mathbb{1} & \sigma_x \\ \sigma_x & -\mathbb{1} \end{pmatrix}, \end{aligned} \quad (\text{S32})$$

which are outlined in [39].

However, the $\tilde{\chi}$ matrix derived this way does not necessarily describe a physical process since a noisy signal may produce a $\tilde{\chi}$ that does not satisfy hermiticity and completeness. To find a χ that satisfies these requirements we apply a most likelihood procedure. This allows us to find a χ which is most likely to produce the observed experimental signal p (A description of this procedure is given in [40]). In the most likelihood estimation we parametrized χ by $\chi(\vec{q})$ to ensure non-negativity and hermiticity[41].

$$\chi(\vec{q}) = \frac{Q^\dagger Q}{\text{Tr}[Q^\dagger Q]}, \text{ with } Q = \begin{pmatrix} q_1 & 0 & 0 & 0 \\ q_5 + iq_6 & q_2 & 0 & 0 \\ q_{11} + iq_{12} & q_7 + iq_8 & q_3 & 0 \\ q_{15} + iq_{16} & q_{13} + iq_{14} & q_9 + iq_{10} & q_4 \end{pmatrix} \quad (\text{S33})$$

Using this parametrization for χ we can now minimize the square residual function defined by

$$\begin{aligned} S(\vec{q}) &= \sum_{a=1}^{d^2} \sum_{b=1}^{d^2-1} \left(p_{a,b} - \sum_{n,m=0}^{d^2-1} \chi_{n,m}(\vec{q}) \langle \varphi_b | A_n | \phi_a \rangle \langle \phi_a | A_m^\dagger | \varphi_b \rangle \right)^2 \\ &+ \lambda \left(\sum_{m,n,k=0}^{d^2-1} \chi_{n,m}(\vec{q}) \text{Tr}(A_m A_k A_n) - \delta_{k,0} \right), \end{aligned} \quad (\text{S34})$$

where $p_{a,b}$ denotes the measurement outcome for a state prepared in $|\phi_a\rangle$ ($|\phi_a\rangle = \{|\downarrow\rangle, |\uparrow\rangle, |x\rangle, |y\rangle\}$) and projected on $|\varphi_b\rangle$ ($|\varphi_b\rangle = \{|\downarrow\rangle, |x\rangle, |y\rangle\}$). The second part of the formula constrains $\chi(\vec{q})$ to be completely positive, with λ a parameter to describe the degree of positivity (a way to find a good starting point \vec{q}_0 is described in ref. [41]).

Using this most likelihood procedure we can find a χ matrix

$$\chi = \begin{pmatrix} 0.81 & -0.02i & -0.01 - 0.01i & -0.01i \\ 0.02i & 0.02 & 0 & 0.02 + 0.01i \\ -0.01 + 0.01i & 0 & 0.14 & 0 \\ 0.01i & 0.02 - 0.01i & 0 & 0.03 \end{pmatrix}. \quad (\text{S35})$$

that is associated with our experimental observations. By using a Monte Carlo simulation we can estimate the error bars associated with the χ matrix found from our most likelihood procedure

$$\delta\chi = \begin{pmatrix} 0.08 & 0.01 + 0.04i & 0.01 + 0.01i & 0.01 + 0.02i \\ 0.01 - 0.04i & 0.06 & 0.01 + 0.01i & 0.01 + 0.01i \\ 0.01 - 0.01i & 0.01 - 0.01i & 0.04 & 0.01 + 0.01i \\ 0.01 - 0.02i & 0.01 - 0.01i & 0.01 - 0.01i & 0.04 \end{pmatrix}. \quad (\text{S36})$$

For this χ matrix all the off diagonal elements are zero within the error bars indicating that $\{\mathbb{1}, \sigma_x, \sigma_y, \sigma_z\}$ is a eigen-basis. In this form the Kraus operators have the physical interpretation of quantum channels. That the largest contribution in χ with $(81 \pm 8)\%$ is associated with the identity $\mathbb{1}$ as expected for a memory. The error channels are $(14 \pm 4)\%$ for phase-bit flip error σ_y , $(2 \pm 6)\%$ for bit flip σ_x and $(3 \pm 4)\%$ for phase flip σ_z error. In the case of only a depolarization channel one would expect an equal distribution between σ_x , σ_y and σ_z . This mismatch can be explained by taking a finite detuning in the RF transition frequency and the fixed chirality of the MREV-8 sequence into consideration.

As discussed in [42] diagonalizing χ allows us to extract a master equation under the assumption that the noise environment is Markovian. The average fidelity calculated based on the solution of the master equation is shown in S12. The results of the extracted master equation are in agreement with the recorded data (blue points) within statistical errors.

The process fidelity F_p associated with the Kraus map χ is defined [40] by $F_p = \text{Tr}(\chi \cdot \chi_{id}) = \chi_{00}$, where χ_{id} is the process matrix representing the identity. Using the relationship [43] between process fidelity F_p and average fidelity $\bar{F} = (d \cdot F_p + 1)/(d + 1)$ we find $\bar{F} = (87 \pm 5)\%$.

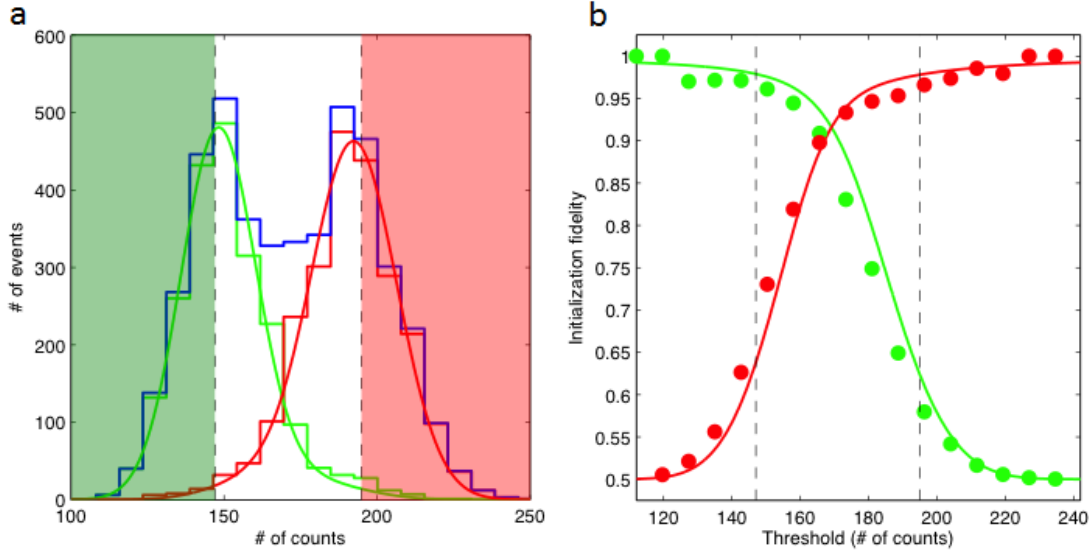


FIG. S1: — **Photon count statistics and initialization fidelity** **a**, shows the photon counting statistics after initialization of the nuclear spin to $|\downarrow\rangle$ (green) and $|\uparrow\rangle$ (red). The histograms are measured data and the solid lines are theory fit. The blue histogram is the total distribution. The green(red) area indicates count rates for which the nuclear spin is initialized in $|\downarrow\rangle$ ($|\uparrow\rangle$). **b**, shows the initialization fidelity of the nuclear spin in $|\downarrow\rangle$ ($|\uparrow\rangle$) green(red) as function of threshold. The points are extracted from the histogram in **a**, the lines are preparation fidelity extracted from the fits in **a**.

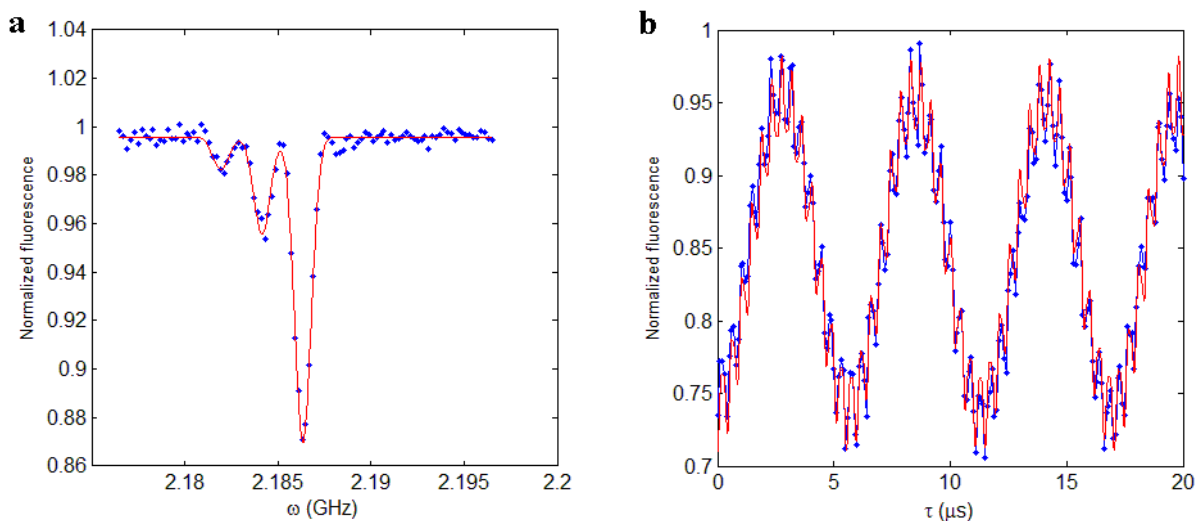


FIG. S2: — **Dynamic Nuclear Polarization.** **a**, ESR scan of $^{14}\text{NV}^-$ center. **b**, Electron Ramsey experiment showing three beating frequencies of hyperfine transitions with significant polarization.

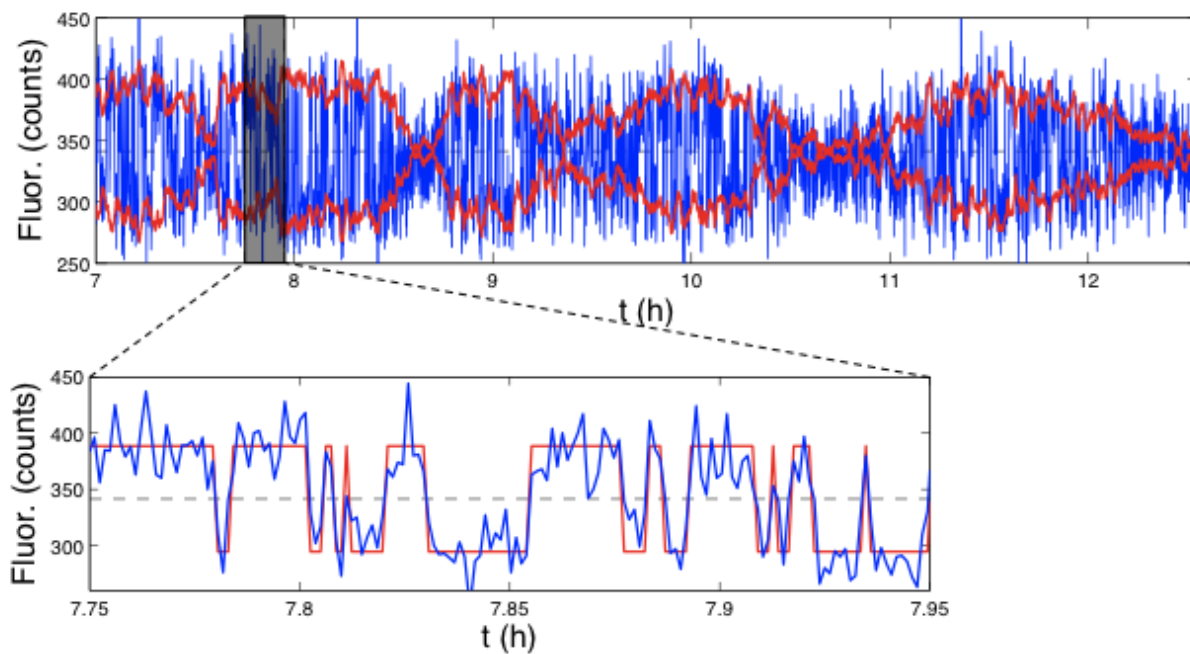


FIG. S3: — **Fluorescence signal as function of time.** Each point of the blue line is an average of 20,000 repetitive readout. The red line shows the envelope of the fluorescence signal. The zoom in reveals individual quantum jumps.

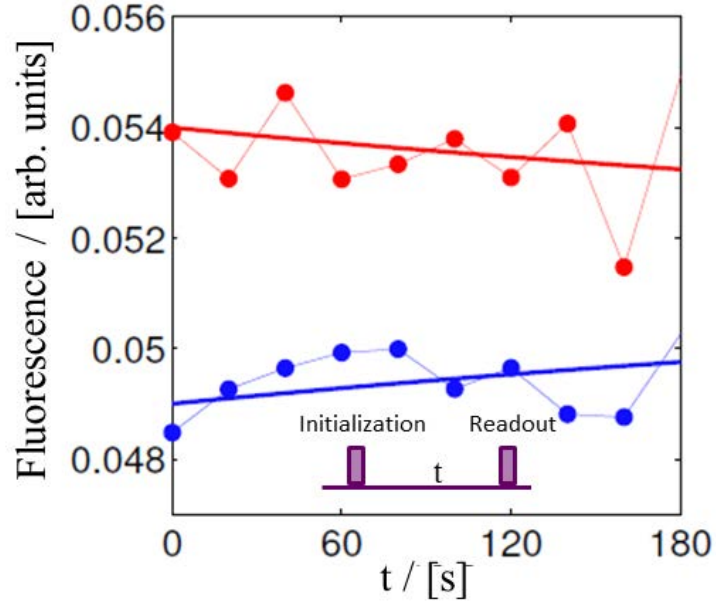


FIG. S4: — T_{1n} time of the ^{13}C nuclear spin in the dark Blue (red) data points correspond to the fluorescence for the nuclear spin initialized to $|\downarrow\rangle(|\uparrow\rangle)$ and waiting time t . The solid lines indicate the nuclear polarization predicted by eq. (S16) with $D_{dd} = (2\pi)0.5$ Hz.

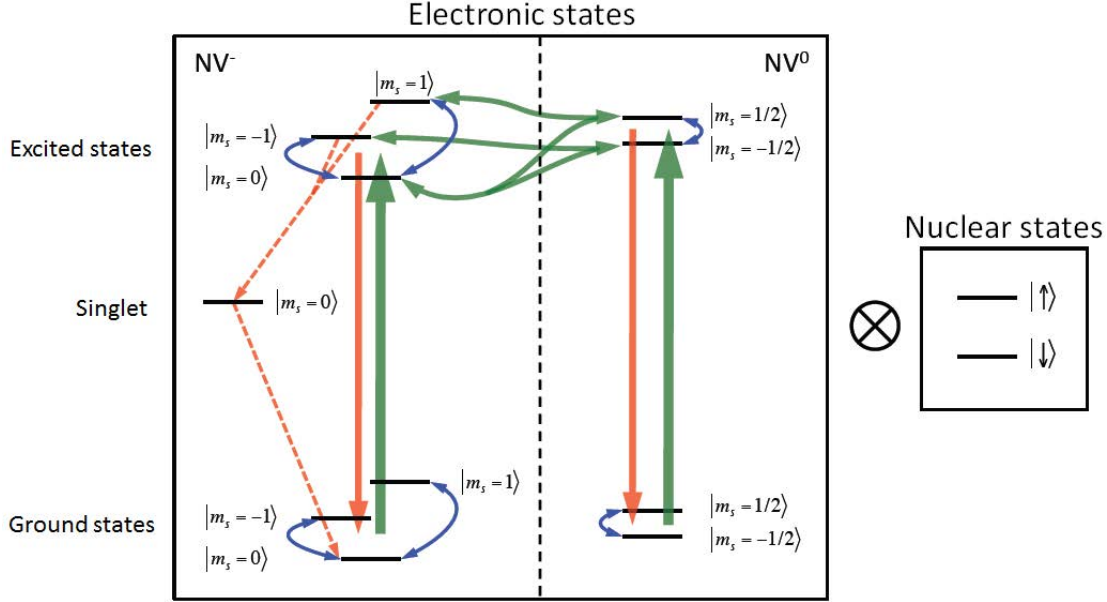


FIG. S5: — Schematic level diagram for an NV center (left box) and a ^{13}C nuclear spin (right box) under illumination with green laser light. The green arrows indicate optical transitions addressed by our green laser pulse, red arrows show electronic decay and blue arrows indicate depolarization of the electronic spin. The transition rates for NV^- employed in our model are taken from ref [33] with the decay rate from the electronic excited state to the ground state $\tilde{\gamma} = \frac{1}{13 ns}$, the decay rate from the singlet to $m_s = 0$ of the electronic ground state $\Gamma = \frac{1}{300 ns}$ and the decay rate from the electronic excited state with $m_s = \pm 1$ to the singlet $\tilde{\gamma}_b = 0.3\tilde{\gamma}$. Moreover we assumed the decay rate of the excited state of NV^0 to be on the same order as for NV^- . The deionization rate from NV^- to NV^0 is taken to be $\gamma_1 = \frac{I/I_{sat}}{70 ns}$ and the ionization rate $\gamma_2 = 2\gamma_1$. The depolarization time for the electronic spin for NV^- is taken to be $T_{1e}^{\text{NV}^-} = 8ms$ and for the case of NV^0 $T_{1e}^{\text{NV}^0} = 6\mu s$ [20]. All the remaining rates are taken to be zero.

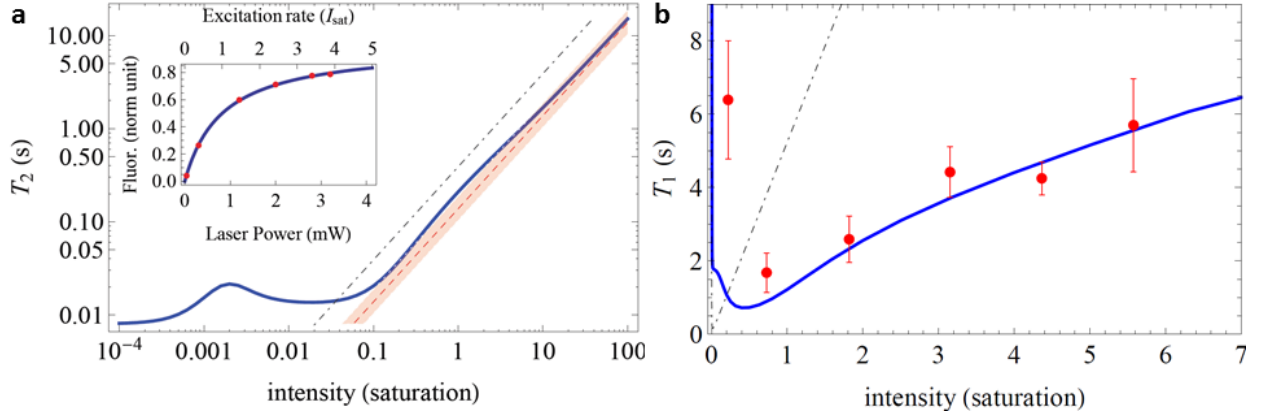


FIG. S6: — **Coherence and T_{1n} time of the ^{13}C nuclear spin** Solution of a master equation (blue) employing the level scheme and transition rates shown in Fig. S5. **a** The initial slope extracted from the measured data is represented by the red dashed line with error bars (red area). To convert the measured slope from Fig. 3 of the main text from laser power (mW) to intensity in units of I_{sat} the saturation curve shown in the inset is used. The dashed-dotted black line is the eq. (S13) with $A_{\parallel} = (2\pi)2.7$ kHz. **b** The red points show the measured nuclear T_{1n} times. The dashed-dotted black line is the solution of eq. (S15) with γ same as is the inset of **a** and $A_{\perp} = (2\pi)1.8$ kHz. The simulated blue line uses A_{\perp} as a fitting parameter.

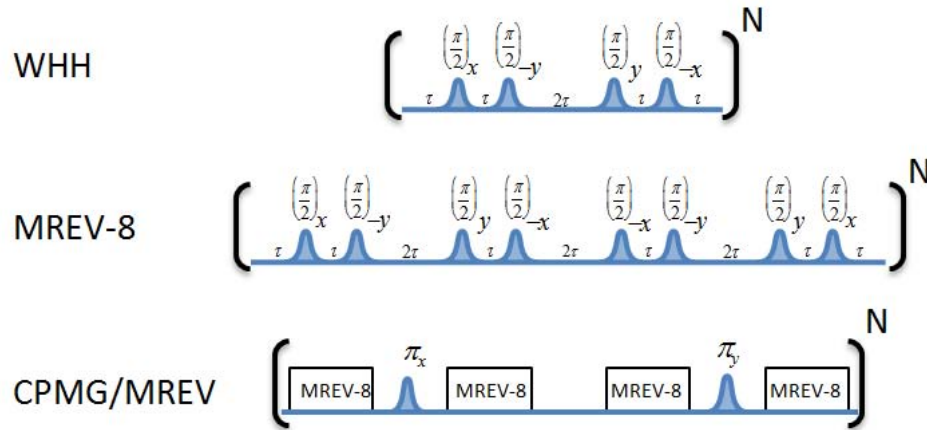


FIG. S7: — **Pulse sequences for decoupling** WHH sequence, showing four RF pulses around the indicated axes for dipole-dipole decoupling. MREV-8 sequence used for increased robustness against pulse errors in WHH. CPMG/MREV sequence adds decoupling from external magnetic field due to additional π -pulses.

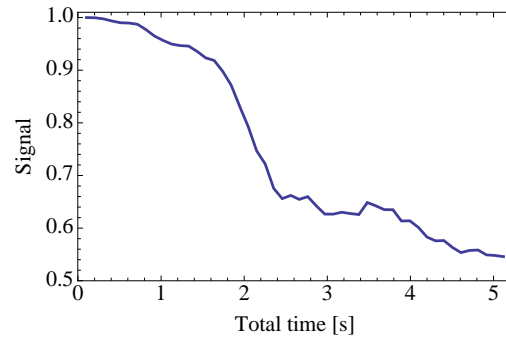


FIG. S8: Signal calculated numerically for 5 bath nuclear spins distributed around the central nuclear spin, assuming 0.01% ^{13}C nuclear spins in the diamond lattice. We assumed constant detuning $\delta/2\pi = 10$ Hz, and averaged over 50 random placements of the surrounding.

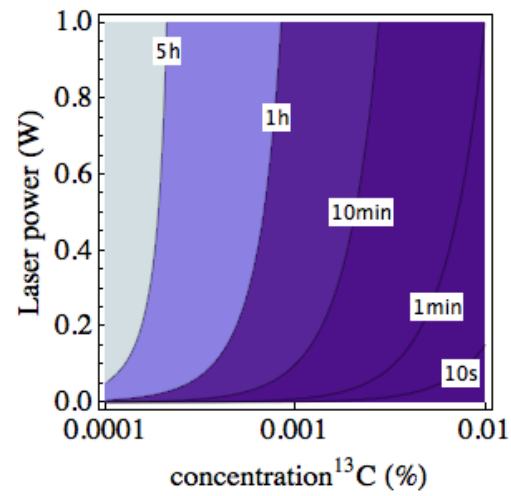


FIG. S9: — **Estimated nuclear coherence time** as a function of laser power and ^{13}C concentration. The hyperfine interaction is chosen to scale proportionally to the ^{13}C concentration.

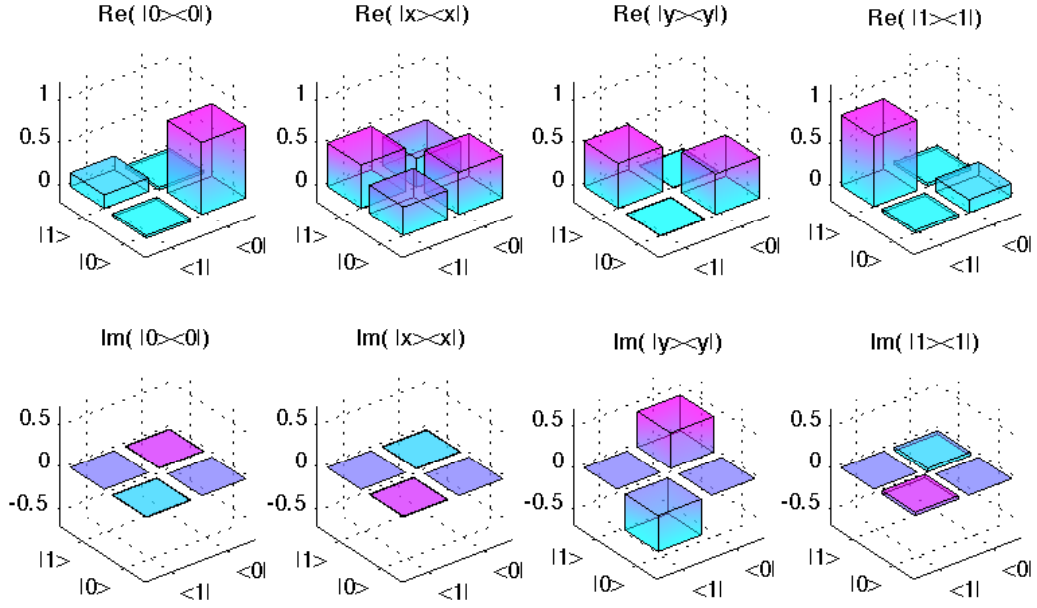


FIG. S10: — **State tomography** The states shown in the figure are $|\downarrow\rangle$, $|x\rangle$, $|y\rangle$ and $|\uparrow\rangle$ after 1 s of storage time.

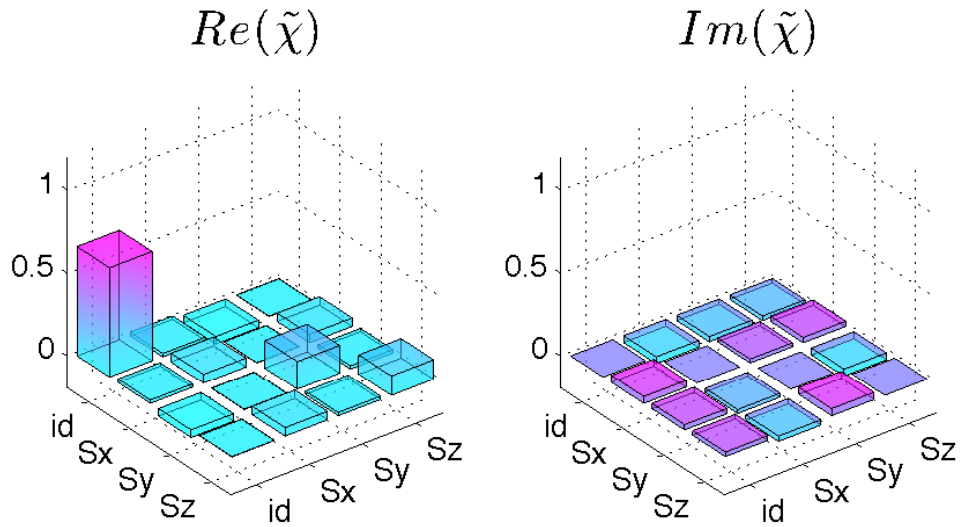


FIG. S11: — **Estimated $\tilde{\chi}$ matrix** Initial reconstruction of the $\tilde{\chi}$ matrix.

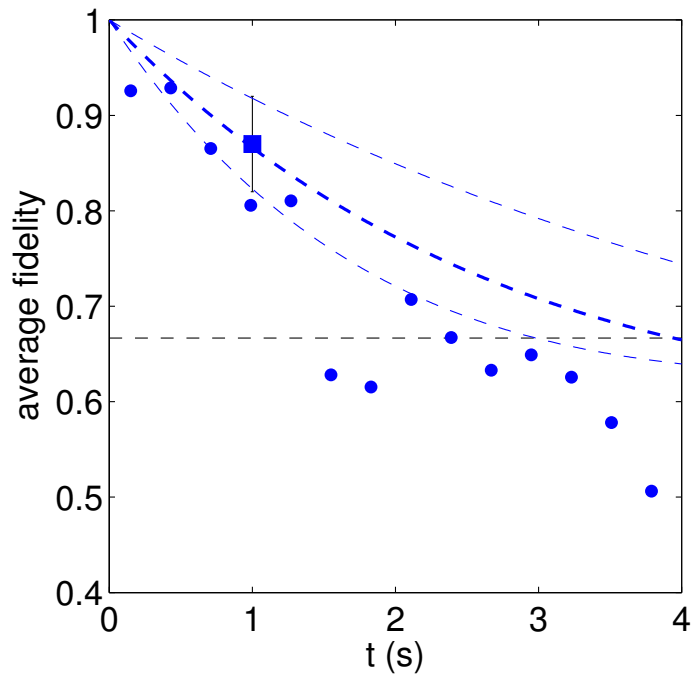


FIG. S12: — **Solution of master equation** The blue points are the measured average fidelity from Fig 4a of the main text. The blue square represents the average fidelity calculated from the χ matrix. The blue dashed line is the average fidelity extracted from the master equation corresponding to blue square.

References and Notes

1. L. M. Duan, C. Monroe, Colloquium: Quantum networks with trapped ions. *Rev. Mod. Phys.* **82**, 1209 (2010). [doi:10.1103/RevModPhys.82.1209](https://doi.org/10.1103/RevModPhys.82.1209)
2. T. D. Ladd *et al.*, Quantum computers. *Nature* **464**, 45 (2010). [doi:10.1038/nature08812](https://doi.org/10.1038/nature08812) [Medline](#)
3. C. Langer *et al.*, Long-lived qubit memory using atomic ions. *Phys. Rev. Lett.* **95**, 060502 (2005). [doi:10.1103/PhysRevLett.95.060502](https://doi.org/10.1103/PhysRevLett.95.060502) [Medline](#)
4. T. D. Ladd, D. Maryenko, Y. Yamamoto, E. Abe, K. Itoh, Coherence time of decoupled nuclear spins in silicon. *Phys. Rev. B* **71**, 014401 (2005). [doi:10.1103/PhysRevB.71.014401](https://doi.org/10.1103/PhysRevB.71.014401)
5. M. V. Balabas, T. Karaulanov, M. P. Ledbetter, D. Budker, Polarized alkali-metal vapor with minute-long transverse spin-relaxation time. *Phys. Rev. Lett.* **105**, 070801 (2010). [doi:10.1103/PhysRevLett.105.070801](https://doi.org/10.1103/PhysRevLett.105.070801) [Medline](#)
6. A. M. Tyryshkin *et al.*, Electron spin coherence exceeding seconds in high-purity silicon. *Nat. Mater.* **11**, 143 (2011). [doi:10.1038/nmat3182](https://doi.org/10.1038/nmat3182) [Medline](#)
7. A. Morello *et al.*, Single-shot readout of an electron spin in silicon. *Nature* **467**, 687 (2010). [doi:10.1038/nature09392](https://doi.org/10.1038/nature09392) [Medline](#)
8. M. V. Gurudev Dutt *et al.*, *Science* **316**, 1312 (2007).
9. T. van der Sar *et al.*, <http://arxiv.org/abs/arXiv:1202.4379v1> (2012).
10. P. Neumann *et al.*, Single-shot readout of a single nuclear spin. *Science* **329**, 542 (2010). [doi:10.1126/science.1189075](https://doi.org/10.1126/science.1189075) [Medline](#)
11. G. de Lange, Z. H. Wang, D. Ristè, V. V. Dobrovitski, R. Hanson, Universal dynamical decoupling of a single solid-state spin from a spin bath. *Science* **330**, 60 (2010). [doi:10.1126/science.1192739](https://doi.org/10.1126/science.1192739) [Medline](#)
12. J. T. Barreiro *et al.*, An open-system quantum simulator with trapped ions. *Nature* **470**, 486 (2011). [doi:10.1038/nature09801](https://doi.org/10.1038/nature09801) [Medline](#)
13. H. Krauter *et al.*, Entanglement generated by dissipation and steady state entanglement of two macroscopic objects. *Phys. Rev. Lett.* **107**, 080503 (2011). [doi:10.1103/PhysRevLett.107.080503](https://doi.org/10.1103/PhysRevLett.107.080503) [Medline](#)
14. G. Balasubramanian *et al.*, Ultralong spin coherence time in isotopically engineered diamond. *Nat. Mater.* **8**, 383 (2009). [doi:10.1038/nmat2420](https://doi.org/10.1038/nmat2420) [Medline](#)
15. Materials and methods are available as supplementary materials on *Science Online*.
16. A. H. Burrell, D. J. Szwer, S. C. Webster, D. M. Lucas, Scalable simultaneous multiqubit readout with 99.99% single-shot fidelity. *Phys. Rev. A* **81**, 040302 (2010). [doi:10.1103/PhysRevA.81.040302](https://doi.org/10.1103/PhysRevA.81.040302)
17. L. Jiang *et al.*, Coherence of an optically illuminated single nuclear spin qubit. *Phys. Rev. Lett.* **100**, 073001 (2008). [doi:10.1103/PhysRevLett.100.073001](https://doi.org/10.1103/PhysRevLett.100.073001) [Medline](#)

18. L. Jiang *et al.*, Repetitive readout of a single electronic spin via quantum logic with nuclear spin ancillae. *Science* **326**, 267 (2009). [doi:10.1126/science.1176496](https://doi.org/10.1126/science.1176496) [Medline](#)
19. P. Neumann *et al.*, Multipartite entanglement among single spins in diamond. *Science* **320**, 1326 (2008). [doi:10.1126/science.1157233](https://doi.org/10.1126/science.1157233) [Medline](#)
20. G. Waldherr *et al.*, Dark states of single nitrogen-vacancy centers in diamond unraveled by single shot NMR. *Phys. Rev. Lett.* **106**, 157601 (2011). [doi:10.1103/PhysRevLett.106.157601](https://doi.org/10.1103/PhysRevLett.106.157601) [Medline](#)
21. V. M. Acosta *et al.*, Temperature dependence of the nitrogen-vacancy magnetic resonance in diamond. *Phys. Rev. Lett* **104**, 070801 (2010). [doi:10.1103/PhysRevLett.104.070801](https://doi.org/10.1103/PhysRevLett.104.070801) [Medline](#)
22. N. Khaneja, R. Brockett, R. J. Glaser, Time optimal control in spin systems. *Phys. Rev. A* **63**, 032308 (2001). [doi:10.1103/PhysRevA.63.032308](https://doi.org/10.1103/PhysRevA.63.032308)
23. C. J. Terblanche, E. C. Reynhardt, J. A. van Wyk, ¹³C spin-lattice relaxation in natural diamond: Zeeman relaxation at 4.7 T and 300 K due to fixed paramagnetic nitrogen defects. *Solid State Nucl. Magn. Reson.* **20**, 1 (2001). [doi:10.1006/snmr.2001.0026](https://doi.org/10.1006/snmr.2001.0026) [Medline](#)
24. S. Wiesner, Conjugate coding. *ACM SIGACT News* **15**, 78 (1983). [doi:10.1145/1008908.1008920](https://doi.org/10.1145/1008908.1008920)
25. F. Pastawski, N. Y. Yao, L. Jiang, M. D. Lukin, J. I. Cirac, Unforgeable noise-tolerant quantum tokens. <http://arxiv.org/abs/1112.5456v1> (2011).
26. D. M. Toyli, C. D. Weis, G. D. Fuchs, T. Schenkel, D. D. Awschalom, Chip-scale nanofabrication of single spins and spin arrays in diamond. *Nano Lett.* **10**, 3168 (2010).
27. P. Spinicelli *et al.*, Engineered arrays of nitrogen-vacancy color centers in diamond based on implantation of CN⁻ molecules through nanoapertures. *New J. Phys.* **13**, 025014 (2011). [doi:10.1088/1367-2630/13/2/025014](https://doi.org/10.1088/1367-2630/13/2/025014)
28. N. Y. Yao *et al.*, Scalable architecture for a room temperature solid-state quantum information processor. *Nat. Commun.* **3**, 800 (2012).
29. P. Neumann *et al.*, Quantum register based on coupled electron spins in a room-temperature solid. *Nat. Phys.* **6**, 249 (2010). [doi:10.1038/nphys1536](https://doi.org/10.1038/nphys1536)
30. E. Togan *et al.*, Quantum entanglement between an optical photon and a solid-state spin qubit. *Nature* **466**, 730 (2010). [doi:10.1038/nature09256](https://doi.org/10.1038/nature09256) [Medline](#)
31. H. Lee, E. Sun, D. Ham, R. Weissleder, Chip-NMR biosensor for detection and molecular analysis of cells. *Nat. Med.* **14**, 869 (2008). [doi:10.1038/nm.1711](https://doi.org/10.1038/nm.1711)
32. V. Jacques *et al.*, Dynamic polarization of single nuclear spins by optical pumping of nitrogen-vacancy color centers in diamond at room temperature. *Phys. Rev. Lett.* **102**, 057403 (2009). [doi:10.1103/PhysRevLett.102.057403](https://doi.org/10.1103/PhysRevLett.102.057403) [Medline](#)
33. N. B. Manson, J. P. Harrison, M. J. Sellars, Nitrogen-vacancy center in diamond: Model of the electronic structure and associated dynamics. *Phys. Rev. B* **74**, 104303 (2006). [doi:10.1103/PhysRevB.74.104303](https://doi.org/10.1103/PhysRevB.74.104303)

34. R. J. Schoelkopf, A. A. Clerk, S. M. Girvin, K. W. Lehnert, M. H. Devoret, <http://arxiv.org/abs/condmat/0210247> (2002).
35. W. M. Itano, D. J. Heinzen, J. J. Bollinger, D. J. Wineland, Quantum Zeno effect. *Phys. Rev. A* **41**, 2295 (1990). [doi:10.1103/PhysRevA.41.2295](https://doi.org/10.1103/PhysRevA.41.2295) [Medline](#)
36. A. Gali, M. Fyta, E. Kaxiras, Ab initio supercell calculations on nitrogen-vacancy center in diamond: Electronic structure and hyperfine tensors. *Phys. Rev. B* **77**, 155206 (2008). [doi:10.1103/PhysRevB.77.155206](https://doi.org/10.1103/PhysRevB.77.155206)
37. M. Mehring, *High Resolution NMR in Solids* (Springer-Verlag, Berlin, 2005).
38. J. M. Taylor *et al.*, High-sensitivity diamond magnetometer with nanoscale resolution. *Nat. Phys.* **4**, 810 (2008). [doi:10.1038/nphys1075](https://doi.org/10.1038/nphys1075)
39. M. A. Nielsen, I. L. Chuang, *Quantum Computation and Quantum Information* (Cambridge Univ. Press, Cambridge, 2000).
40. J. L. O'Brien *et al.*, Quantum process tomography of a controlled-NOT gate. *Phys. Rev. Lett.* **93**, 080502 (2004). [doi:10.1103/PhysRevLett.93.080502](https://doi.org/10.1103/PhysRevLett.93.080502) [Medline](#)
41. D. F. V. James, P. G. Kwiat, W. J. Munro, A. G. White, Measurement of qubits. *Phys. Rev. A* **64**, 052312 (2001). [doi:10.1103/PhysRevA.64.052312](https://doi.org/10.1103/PhysRevA.64.052312)
42. S. Haroche, J. M. Raimond, *Exploring the Quantum: Atoms, Cavities and Photons* (Oxford Univ. Press, Oxford, 2006).
43. M. A. Nielsen, *Phys. Rev. A* **303**, 249 (2002).